Covariations between the Indian Ocean dipole and ENSO: a modeling study

Hui Wang[1], Arun Kumar[1], Raghu Murtugudde[2], Balachandrudu Narapusetty[1,2,3], Knut L. Seip[4]

[1] NOAA/NWS/NCEP/Climate Prediction Center, College Park, Maryland, USA

[2] ESSIC, University of Maryland, College Park, Maryland, USA

[3] Innovim, Greenbelt, Maryland, USA

[4] Faculty of Technology, Art, and Design, OsloMet – Oslo Metropolitan University, Oslo, Norway

Climate Dynamics

Manuscript submitted on 30 May 2018 and revised on 26 April 2019 and 21 June 2019

Corresponding author address:

Hui Wang, NOAA Climate Prediction Center, 5830 University Research Court, NCWCP, College Park, MD 20740, USA

e-mail: hui.wang@noaa.gov

Abstract

The coevolution of the Indian Ocean dipole (IOD) and El Niño-Southern Oscillation (ENSO) is examined using both observational data and coupled global climate model simulations. The covariability of IOD and ENSO is analyzed by applying the extended empirical orthogonal function (EEOF) method to the surface and subsurface ocean temperatures in the tropical Indian Ocean and western Pacific. The first EEOF mode shows the evolution of IOD that lags ENSO, whereas the second mode exhibits the transition from a dipole mode to a basin-wide mode in the tropical Indian Ocean that leads ENSO. The lead-lag relationships between IOD and ENSO are consistent with two-way interactions between them. A comparison between two 500-year model simulations with and without ENSO shows that ENSO can enhance the variability of IOD at interannual time scale. The influence of ENSO on the IOD intensity is larger for the eastern pole than for the western pole, and further, is stronger in the negative IOD phase than in the positive phase. The influence of IOD on ENSO is demonstrated by the improvement of ENSO prediction using sea surface temperature (SST) in the tropical Indian Ocean as an ENSO precursor. The improvement of the ENSO forecast skill is found at both a short lead time (0 month) and long leads (10–15 months). The SST in the western pole has more predictive value than in the eastern pole. The eastward propagation of surface and subsurface temperature signals from the western Indian Ocean that precedes the development of heat content anomaly in the tropical western Pacific is the key for extending the lead time for ENSO prediction. Our results are consistent with previously reported findings but highlight the spatial-temporal evolution of the ENSO-IOD system. It is also illustrated that IOD would have been more helpful in predicting the 1997/98 El Niño than the 2015/16 El Niño.

Keywords Indian Ocean dipole, El Niño-Southern Oscillation (ENSO), Climate modeling

1. Introduction

The Indian Ocean dipole (IOD) is an intrinsic mode of variability of the tropical Indian Ocean (Saji et al. 1999; Webster et al. 1999; Murtugudde et al. 2000; Ashok et al. 2003a; Behera et al. 2006; Luo et al. 2008, 2010; Du et al. 2013; Wang et al. 2016; Saji 2018). It has broad impacts on regional climate (e.g., Ashok et al. 2001, 2003b, 2004; Annamalai and Murtugudde 2004; Li and Mu 2001; Xiao et al. 2002; Saji and Yamagata 2003a; Behera et al. 2005; Tamura et al. 2011; Cherchi and Navarra 2013). An important issue in the studies of IOD is the relationship between IOD and the El Niño-Southern Oscillation (ENSO). Previous studies have shown that the development of IOD can be independent of ENSO, but ENSO may also exert significant influence (Saji et al. 1999; Webster et al. 1999; Allan et al. 2001; Annamalai et al. 2003; Wang et al. 2004; Drbohlav et al. 2007; Stuecker et al. 2017). In recent years, it has also been found that IOD can affect ENSO (Izumo et al. 2010, 2014, 2016; Zhou et al. 2015; Jourdain et al. 2016). Clearly, there exist two-way interactions between IOD and ENSO.

Figure 1 shows the spatial distribution of seasonal mean sea surface temperature (SST) anomaly in September, October, and November (SON) of 1997 and 2015, which is the peak season of the IOD life cycle. In the eastern equatorial Pacific, SST anomalies were observed well above 3 K even before the winter season in both years, leading to descriptors like Super El Niños. In the meantime, there was a dipole in the tropical Indian Ocean, with warm SST anomalies in the western Indian Ocean (WIO) and cold anomalies in the eastern Indian Ocean (EIO). Noticeably, both El Niño events were accompanied by an IOD in its positive phase although IOD was relatively weak during 2015, where the IOD index (e.g., Saji et al. 1999) is defined as the difference between SST anomalies averaged over the WIO (50^o–70^oE, 10^oS–10^oN) and EIO (90^o–110^oE, 10^oS–Eq.).

Although a positive (negative) IOD tends to co-occur with El Niño (La Niña) as shown in Fig. 1, which is also found in previous studies (e.g., Annamalai et al. 2003; Behera et al. 2006; Luo et al. 2010), the spatial-temporal covariations of the two major climate modes in the tropical Pacific and Indian Oceans have not been well documented; particularly, in terms of their two-way interactions. Several studies have demonstrated that the state of IOD may help predict the following year's ENSO, and thus extend the forecast lead time to longer than a year (Wu and Kirtman 2004; Annamalai 2005; Izumo et al. 2010; Dayan et al. 2014; Jourdain et al. 2016). It would be interesting to know whether IOD can help predict a major El Niño like the 1997/98 and 2015/16 events at a lead time longer than current operational seasonal forecasts (9–10 months). It would also be interesting to know the relative importance of the eastern and western poles to the ENSO prediction.

A recent modeling study by Wang et al. (2016) proposed a forcing mechanism for IOD in the absence of ENSO. After suppressing the ENSO-related SST variability in a coupled model and based on the analysis of a 500-year simulation, they showed that the SST anomaly in EIO associated with IOD can be generated through local low-level wind response to springtime Indonesian rainfall anomaly. The time evolution of IOD without ENSO, together with the associated tropical Indian Ocean subsurface variability was also documented.

This study is aimed at examining the evolution of IOD in the presence of ENSO. The present work complements the analysis of Wang et al. (2016) by analyzing the spatial-temporal covariations between IOD and ENSO, characterizing lead and lag relationships between them, and quantifying the influence of ENSO. This is achieved by analyzing a 500-year long fully coupled model simulation, which retains the ENSO mode of variability (referred to as ENSO run hereafter), and comparing the results with the 500-year simulation in which the ENSO mode is suppressed (referred to as no-ENSO run hereafter). The latter was analyzed and presented in Wang et al. (2016) to investigate the forcing mechanism and to characterize the spatial-temporal evolution of IOD in the absence of ENSO. The differences in the characteristics of IOD between the two simulations quantify the impact of ENSO on IOD.

This paper is organized as follows. Section 2 provides brief descriptions of the data, model, and experimental design. The coevolution between IOD and ENSO is examined in Section 3, including both the impact of ENSO on IOD and the influence of IOD on ENSO prediction. Conclusions are presented in Section 4.

2. Data, model and experimental design

The data used in this study consist of precipitation, SST, subsurface ocean temperature, warm water volume (WWV), and 10-m wind. They are taken from observations (including reanalysis data) and model simulations. Observational SSTs are obtained from the National Oceanic and Atmospheric Administration (NOAA) Optimum Interpolation SST version 2 (OISSTv2; Reynolds et al. 2002) on a $1^{\circ} \times 1^{\circ}$ (latitude × longitude) grid. The WWV is defined as the volume of water warmer than 20°C in the tropical Pacific (120°E–80°W, 5°S–5°N) and derived based on ocean temperature profiles from TAO moorings (Meinen and McPhaden 2000; data available at http://www.pmel.noaa.gov/tao/wwv/data/wwv.dat). Both SST and WWV data are monthly means from 1982 to 2016. The subsurface ocean temperatures are taken from an ocean reanalysis dataset, namely, the National Centers for Environmental Prediction's (NCEP) Global Ocean Data Assimilation System (GODAS; Behringer and Xue 2004). GODAS has a horizontal resolution of $0.333^{\circ} \times 1^{\circ}$ (latitude × longitude) and 40 layers from 5 m below sea level to 4478 m depth with 20 layers in the upper 200 m. The GODAS dataset covers a 36-year period from 1980 to 2015.

To assess the impact of ENSO on IOD, we analyze and compare two 500-year simulations with and without the ENSO mode, similar to Behera et al. (2006). The simulations were conducted with the NCEP Climate Forecast System version 1 (CFSv1; Saha et al. 2006). The coupled model consists of atmosphere, ocean, and land components. They are the NCEP Global Forecast System (GFS) version 1 (Moorthi et al. 2001), the Geophysical Fluid Dynamics Laboratory (GFDL) Modular Ocean Model version 3 (MOM3; Pacanowski and Griffies 1998), and the Oregon State University (OSU) land surface model (LSM; Pan and Mahrt 1987), respectively. The atmospheric model has T62 horizontal resolution and 64 vertical levels. The ocean model covers global oceans from 74°S to 64°N with a zonal resolution of 1° and meridional resolutions of 1/3° in the tropics (10°S–10°N) and decreasing to 1° in the extratropics (poleward of 30°S and 30°N). It has 40 vertical layers, same as GODAS. More detailed descriptions of the CFSv1 were given by Saha et al. (2006).

For both the ENSO run and no-ENSO run, the CFSv1 was integrated for 500 years. The ENSO run is a fully coupled simulation which allows air-sea interaction and retains the ENSO mode of variability. In the no-ENSO run, ENSO is suppressed by nudging the model daily SST (SST_{MOM3}) to an observed daily SST climatology (SST_{OBS}) in the tropical Pacific (140°E–75°W, 10°S–10°N). The resultant new SST (SST_{NEW}) is

$$SST_{NEW} = (1 - w) \times SST_{MOM3} + w \times SST_{OBS},$$

where w is a weighting coefficient, which is 1/3 in the domain of (140°E–75°W, 10°S–10°N) and is linearly reduced to 0 on the border of a larger domain (130°E–65°W, 15°S–15°N). The daily SST climatology was interpolated from the long-term mean (1981–2008) monthly SST of the NOAA OISSTv2 (Reynolds et al. 2002) dataset. Using $w = 1/3$, the model SST is relaxed to the observed climatology with an e-folding time of 3.3 days, which effectively removes the interannual variability of SST in the tropical Pacific and El Niño/La Niña as well. This set of two 500-year simulations has been employed for the studies of the ENSO diversity (Kim et al. 2012), the Pacific decadal oscillation (Wang et al. 2012a, 2012b; Kumar et al. 2013), the IOD (Wang et al. 2016), decadal predictability (Kumar and Wang 2015), and the impact of ENSO on droughts in the Southwest U.S. (Wang and Kumar 2015) and East China (Liu et al. 2017).

The results presented in this study are based on the analysis of the last 480 years of the ENSO run and no-ENSO run. As shown by Wang et al. (2016), in the absence of ENSO, the IOD in the no-ENSO run possesses some of the fundamental features of the observed IOD. Therefore, the differences in the characteristics of IOD between the two simulations may indicate the impact of ENSO on IOD.

3. Results

3.1 Covariations between IOD and ENSO

The spatial-temporal covariations between IOD and ENSO are examined first by using the extended empirical orthogonal function (EEOF) method (Weare and Nasstrom 1982). The EEOF analysis is based on the spatial-temporal covariance matrix of 480-year monthly mean ocean temperature averaged between 10^{o}S and 5^{o}N to represent tropical ocean temperature variability with a temporal window of 18 months. The longitude–depth domain for the EEOF analysis is from 50^{o}E to 180^o, covering the tropical Indian Ocean and western Pacific, and from 5-m to 225-m depth below the sea surface, thus including both sea surface (5-m depth, the top layer of the ocean model) and subsurface. Unlike ordinary EOFs in which spatially propagating signals need to be described by a pair of EOF modes (e.g., Wang et al. 2013), single EEOF mode can represent propagating features (Weare and Nasstrom 1982).

Figure 2 shows the first EEOF mode (EEOF1) in the form of correlation and regression maps for ocean temperature averaged between 10^{o}S and 5^{o}N from month 0 to month 28. These maps are obtained by correlating and regressing the ocean temperature anomalies against the principal component (PC) time series of EEOF1 for ocean temperature lagging PC1 by 0 month to 28 months. This mode accounts for 31% of surface and subsurface temperature variance in the tropical Indian Ocean and western Pacific.

The time evolution of EEOF1 begins with warm subsurface temperature anomalies in the tropical western Pacific (Fig. 2, month 0). From month 2 to 4, temperature anomalies propagate eastward along the thermocline, generate warm SST anomalies in the eastern and central Pacific, and result in coupled Bjerknes feedback (Bjerknes 1969) and hence an El Niño. In the following months (Fig. 2, months 6–14), the El Niño continues to grow with increases in SST and subsurface temperature anomalies. In the meantime, cold temperature anomalies develop in the tropical western Pacific, as well as in EIO while warm anomalies develop in WIO. The latter two form a positive IOD.

During the decay phase of the El Niño (Fig. 2, months 18–26), warm temperature anomalies in WIO propagate eastward and replace cold anomalies in EIO. As a consequence, a basin-wide warming takes place in both the surface and subsurface tropical Indian Ocean, consistent with the tropical Indian Ocean surface and subsurface responses to El Niño (e.g., Cadet 1985; Klein et al. 1999; Wang et al. 2013). In month 28, EEOF1 ends up with warm temperature anomalies in EIO and cold subsurface temperature anomalies in the western Pacific. The latter favors the development of a La Niña. Figure 2 illustrates that the development of a positive IOD and its transition to a basin-wide warming in the tropical Indian Ocean lag the El Niño.

The second EEOF (EEOF2) is shown in Fig. 3, which accounts for 16% of the surface and subsurface temperature variance. In month 0, there is an El Niño in the tropical Pacific and a positive IOD in the tropical Indian Ocean. Although the magnitudes of the associated temperature anomalies are relatively small (Fig. 3, months 0–10), their spatial structures are like those in EEOF1 (Fig. 2, months 10–20). Also, similar to EEOF1 (Fig. 2, months 18–26), the decay of the El Niño in EEOF2 is associated with the thermocline variability in the tropical Pacific and eastward propagating temperature anomalies in the tropical Indian Ocean, leading to a basin-wide mode (Fig. 3, months 8–16). In month 18 (Fig. 3), the tropical Pacific is characterized by a La Niña with cold temperature anomalies in both the surface and subsurface, whereas EIO is dominated by warm anomalies. In the following months, cold anomalies develop in WIO, leading to a negative IOD. Additionally, there are weak warm anomalies in the western Pacific in month 20. These warm anomalies continue to intensify during months 22–28, shift eastward, and are precursors for the next El Niño. The warm anomalies in the surface and subsurface of the western Pacific come after the warm anomalies in EIO originating from WIO. This suggests that both the IOD and the following basin-wide mode lead the forthcoming El Niño. In month 28 (Fig. 3), the distributions of temperature anomalies in the two tropical basins are out of phase with those in month 0. Figure 3 thus displays a half cycle of the evolutions of IOD and El Niño/La Niña associated with EEOF2.

The two leading EEOF modes capture the covariations between IOD and ENSO that are associated with tropical ocean subsurface variability. In both modes, there are strong links between surface and subsurface temperature anomalies. Each mode represents a distinctive relationship between IOD and ENSO. In the first mode, a positive IOD lags an El Niño. In the second mode, a positive IOD and a basin-wide mode lead the development of warm ocean temperature anomalies in the western Pacific, a precursor for El Niño. Similar lead and lag relationships between IOD and ENSO are also obtained by the EEOF analysis with the 36-year GODAS data (not shown).

The spatial-temporal covariations and the lead-lag relationships between IOD and ENSO depicted by the two EEOFs can also be seen in the SST field. Figures 4 and 5 show the evolution of the SST anomalies associated with EEOF1 and EEOF2, respectively, together with the 10-m wind and precipitation anomalies obtained by regressing the 480-year monthly mean data against the PC1 and PC2 time series. Associated with EEOF1, the development of El Niño (Fig. 4, month 4) precedes the negative precipitation anomalies in Indonesia (month 6) and the easterly and southeasterly wind anomalies in EIO (months 6 and 8), which trigger the onset of IOD (months 8 and 10; Annamalai et al. 2003; Hendon 2003; Wang et al. 2016). The surface wind anomalies (Fig. 4, months 6–12) are a response to dry conditions across Indonesia induced by El Niño through a weakened Walker circulation (Hendon 2003). The basin-wide warming in the tropical Indian Ocean (Fig. 4, months 18–22) is also a response to El Niño (e.g., Latif and Barnett 1995; Wallace et al. 1998; Saji and Yamagata 2003b; Okumura and Deser 2010; Xie et al. 2009). Therefore, EEOF1 reflects the IOD response to ENSO.

In EEOF2, the warm SST anomalies associated with the basin-wide mode move eastward in the tropical Indian Ocean, leading to a reversal in zonal wind over the equatorial Indian Ocean (Fig. 5, months 10–16). Together with the easterly wind anomalies in the western Pacific associated with La Niña, they produce low-level wind convergence and cause positive precipitation anomalies over the Indo-Pacific warm pool (Fig. 5, months 16–20). Warm water also piles up in the same region, which increases SST and deepens the thermocline in the western Pacific (Figs. 3 and 5, months 20–24). The eastward movement of the subsurface warm temperature anomalies from the western Pacific (Fig. 3, month 24–28) is a precursor of an El Niño. It is indeed observed that the development of an El Niño may follow a basin-wide warming in the tropical Indian Ocean (Wu and Kirtman 2004; Annamalai et al. 2005). The second EEOF thus indicates an influence of the tropical Indian Ocean on the western Pacific. The two EEOF modes portray the combined evolution of IOD and El Niño/La Niña together as a coupled system. It is suggested that the IOD and the basin-wide warming in the tropical Indian Ocean may be a response to El Niño, which in turn may help the development of El Niño. Figures 4 and 5 also indicate that the atmospheric circulation links the changes in SST in the two ocean basins. Their two-way interactions are further examined in the following two subsections.

3.2 Impact of ENSO on IOD

3.2.1 Frequency

Based on the analysis of IOD in the no-ENSO run, Wang et al. (2016) demonstrated that ENSO is not fundamental for the existence of IOD. In the absence of ENSO, IOD can be initiated by springtime Indonesian precipitation anomalies through the surface wind response over EIO. To characterize the variability of Indonesian precipitation, Hendon (2003) defined an Indonesian precipitation (IndoP) index by averaging precipitation anomalies over the maritime continent within the domain of (95^{o}E–141^{o}E, 10^{o}S–5^{o}N). The onset of IOD triggered by IndoP was supported by the lagged relationship between spring IndoP and the IOD-related 10-m wind/SST of the following summer and fall (Wang et al. 2016, their Fig. 5). *Given a strong influence of ENSO on Indonesian precipitation (Hendon 2003), IndoP may further act as a medium linking IOD and ENSO.*

Figure 6a shows the power spectra of the IndoP index in both the ENSO run and no-ENSO run, as well as the Niño 3.4 SST index in the ENSO run. To obtain smoothed power spectra, the 480-year time series is divided into eight segments of 60 years. The power spectra shown in Fig. 6 are an average of the spectra computed for the eight individual segments. The statistical significance of spectral peaks is estimated by comparing these peaks to corresponding red-noise spectra.

The power spectrum of the Niño 3.4 index in the ENSO run is characterized by significant peaks at the interannual time scale between 2.5 and 6.5 years. The IndoP in the ENSO run also displays significant peaks at the interannual time scale between 3 and 6 years, consistent with the ENSO forcing. In contrast, the IndoP in the no-ENSO run lacks power at the interannual time scale presumably due to the absence of ENSO in the simulation. Additionally, the IndoP index in both the ENSO run and no-ENSO run shows significant peaks at short time scales (< 2.5 years), which are likely independent of ENSO. Figure 6b shows the power spectra of the IOD index in both the ENSO and no-ENSO runs. The most significant difference between the two is the spectral peak at 4 years in the ENSO run, indicating enhanced IOD variability at interannual time scale by ENSO.

The power spectrum analysis is also applied to the PC time series of EEOF1 and EEOF2 in both the ENSO and no-ENSO runs (Fig. 7). In the ENSO run (Fig. 7a), both EEOF1 and EEOF2 are dominated by the variability at interannual time scale. The spectral peaks are at 5.5 and 4 years for EEOF1 and EEOF2, respectively, which are close to the largest peaks of the Niño 3.4 index (5 years) and the IOD index (4 years, Fig. 6b, red). In the no-ENSO run (Fig. 7b), both EEOF modes (their spatial patterns shown in Figs. 11 and 12 in Wang et al. 2016) are characterized by the spectral peaks at shorter time scales ranging from 1 year to 4 years, consistent with those of the IOD index in the no-ENSO run (Fig. 6b, blue). The power in these spectral peaks (Fig. 7b) is weaker than those in the ENSO run (Fig. 7a).

A comparison between Fig. 7a and 7b reveals that in the absence of ENSO, the variability of IOD, which is represented by the two leading EEOFs in the no-ENSO run (Wang et al. 2016), is confined to a relatively shorter time scale (< 4 years). In the presence of ENSO, there is strong covariability between IOD and ENSO at the interannual time scale. Therefore, the variability of IOD is also significantly enhanced at interannual time scale. The result is consistent with the power spectrum of the IOD index in the ENSO run (Fig. 6b, red).

Whether the results based on the model simulations are reliable is further assessed by comparing the power spectra of the Niño 3.4 index, the IOD index, and the two PC time series in the ENSO run (Figs. 6b, 7a) to those derived from the 36-year GODAS data shown in Fig. 8. Overall, the spectral peaks of these time series in the ENSO run are like those in GODAS. This similarity gives us confidence for evaluating the ENSO influence on IOD with the two simulations. It is also noted that the power spectra of the IOD in GODAS show a minimum power at 2 years (Fig. 8a), which is different from the quasi-biennial variation of the IOD found in previous studies (e.g., Saji et al. 1999). To ascertain the power peaks of IOD from the GODAS analysis, a similar analysis is performed on the IOD index derived from the OISST dataset. The corresponding power spectra (not shown) are very similar to those in Fig. 8a, also with a minimum at 2 years. More discussions on this issue are presented in the Appendix.

3.2.2 Time evolution

As shown in Figs. 2 and 3, the time evolution of EEOF1 from month 12 to month 28 is like that of EEOF2 from month 0 to month 16. This suggests that the covariations between IOD and ENSO involve an alternation between the two EEOF modes. The simultaneous correlation between the two PC time series is zero because of the constraint of orthogonality for the EEOF method. However, the lead-lag correlations between the two PCs are nonzero. Figure 9a shows such lead-lag correlations in both the ENSO run and no-ENSO run, as well as in GODAS.

For the ENSO run (red solid line), the largest positive (negative) correlation is found when PC1 leads (lags) PC2 by about 11 months. For example, the evolution of IOD and ENSO is first dominated by EEOF1 (Fig. 2). A positive IOD follows an El Niño during the developing phase (Fig. 2, months 0–12). When the El Niño reaches its peak intensity in month 14 (Fig. 2), EEOF2 may kick in (Fig. 3) between months 2 and 4 because of the largest positive correlation with an 11-month lag. The covariation of IOD and ENSO continues in the following 22 months (Fig. 3), including the decay of the El Niño from month 4 to month 14 and the development of a La Niña from month 16 to month 24. In the meantime, there is a transition from a positive IOD to a basin-wide warming in the Indian Ocean during month 4 and month 16, followed by a negative IOD from month 18 to month 24 and the warming of the western Pacific subsurface during months 20 and 24. After the 22-month evolution, both IOD and ENSO (Fig. 3, month 26) are opposite to their initial phase when EEOF2 gets started (Fig. 3, month 4). They may continue to evolve and return to EEOF1 (Fig. 2) in month 15 because of the largest negative correlation with an 11-month lag. The conceptual picture of the covariations of ENSO and IOD through the alternation between EEOF1 and EEOF2 is summarized in Fig. 10.

The time interval between the two vertical dashed red lines in Fig. 9a is an estimation of the timescale (11 + 11 = 22 months) for an alternation between the two modes. It also characterizes the timescale of the covariations between IOD and ENSO. This timescale in the ENSO run (22 months) is comparable to the observations (GODAS, 9 + 9 = 18 months), but is longer than that in the no-ENSO run (7 + 5 = 12 months). The difference in the timescale between the ENSO run and no-ENSO run is another indicator of the influence of ENSO on the evolution of IOD.

The covariations of IOD and ENSO via the alternation between the two EEOFs can also be seen in the lead and lag correlations of the Niño 3.4 and IOD indices with the two PC time series of EEOF1 and EEOF2 in the ENSO run, as shown in Fig. 9b. Both the indices correlate with EEOF1 with a maximum correlation when EEOF1 leads the indices by 4 months (orange and blue). The lead and lag correlations of the two indices with EEOF2 (yellow and green) are similar to the lead and lag correlations between EEOF1 and EEOF2 (Fig. 9a, red), with a maximum correlation (positive) when the indices lead EEOF2 and a minimum (negative) when the two indices lag EEOF2. Compared to the correlations of EEOF1 with EEOF2 in Fig. 9a (red), the maxima and minima in Fig. 9b (yellow and green) shift towards right, consistent with the maximum correlations between EEOF1 and the two indices at a 4-month lag (Fig. 9b, orange and blue). The positive maximum and negative minimum correlations with EEOF2 indicate that the phase change for both ENSO and IOD can happen during the evolution of EEOF2 (Fig. 3). The half-cycle time is around 20 months for ENSO and 14 months for IOD, estimated based on the lag interval between the positive and negative extreme correlations, which is consistent with the relatively low-frequency variability of ENSO and higher-frequency variability of IOD (Fig. 6b). It is also obvious that the lead and lag correlations of the Niño 3.4 index with the two PC time series are much stronger than those of the IOD index with the two PCs. The lead and lag correlations between the two indices (Fig. 9b, red) show a maximum of 0.28 when the IOD index leads the Nino 3.4 index by 1 month, suggesting a certain chance of co-occurrence of ENSO and IOD (e.g., Fig. 1).

The co-occurrence of IOD and ENSO is further examined in Table 1 by counting the number of SON seasons during which a positive (negative) IOD co-occurs with an El Niño (La Niña) in the 480-year simulations. Both the ENSO and IOD events are defined with their index value that exceeds their corresponding one standard deviation. In the model simulations, the standard deviations of the 480-year SON Niño 3.4 index and the IOD time series are 0.90 K and 1.20 K, respectively. There are 79 El Niño and 88 La Niña events and 108 positive and 90 negative IOD events. Among them, 29 (35) SON seasons are found with the co-occurrence of a positive (negative) IOD and an El Niño (La Niña), which accounts for 27% and 39% of positive and negative IOD events, respectively. It is also found that 5% of positive IODs and 4% of negative IODs in the model co-occur with La Niña and El Niño, respectively. Such IOD–ENSO combinations also exist in observations (e.g., Saji et al. 1999, their Fig. 1).

3.2.3 Intensity

ENSO not only influences the temporal scale of IOD, but also affects the intensity of IOD. Figure 11 shows the scatter plot of EIO SST anomaly versus WIO SST anomaly in SON, the peak season of IOD, for both the ENSO and no-ENSO runs. It is evident that the amplitudes of these SST anomalies are larger in Fig. 11b than in Fig. 11a, especially in the right lower quadrant during the negative IOD phase. Compared to the no-ENSO run, the SST variance in the ENSO run is increased by 42% and 25%, respectively, in the eastern and western poles of IOD. The variance of the IOD index is increased by 30%. The corresponding increases are 14% (eastern pole), 2% (western pole), and 6% (dipole) when IOD is in a positive phase. In contrast, they are 55%, 50%, and 52% when IOD is in a negative phase. Therefore, the ENSO impact on the IOD intensity is larger for the eastern pole than for the western pole, and is stronger during a negative IOD event than during a positive event. This is consistent with the fact that there is also an east-west asymmetry in the ocean dynamics with a stronger mixed layer-thermocline interaction in the eastern pole than in the western pole (Murtugudde and Busalacchi 1999, Murtugudde et al. 2000). The results, therefore, reveal an asymmetry of the ENSO influence between the positive and negative IOD phases.

3.3 Influence of IOD on ENSO prediction

The impact of IOD on ENSO can be manifested in its influence on the skill of ENSO prediction. Figure 3 illustrates that the evolution of EEOF2 involves eastward propagation of warm temperature anomalies from WIO, followed by the development of warm subsurface temperature anomalies in the western tropical Pacific which in turn leads to an El Niño. The lagged relationship provides a basis for using SST anomaly in WIO as a predictor for ENSO forecast. To demonstrate the feasibility of this hypothesis, a linear regression model is employed to statistically forecast winter seasonal mean (December, January, and February, DJF) Niño 3.4 SST. The forecasts are cross-validated and compared with similar statistical forecasts using WWV as a predictor, as well as the CFSv2 dynamical seasonal forecasts (Saha et al. 2014).

Figure 12 shows the forecast skills assessed by anomaly correlations between the predicted and observed Niño 3.4 SST over 1983–2010, the CFSv2 hindcast period (Saha et al. 2014), for the statistical forecasts using WIO SST and WWV as predictors and the CFSv2 retrospective forecasts (Saha et al. 2014). Both predictors, namely, WIO SST and WWV, are derived from pre-season observations. The former is the average of SSTs over the WIO domain (50^o–70^oE, 10^oS–10^oN) and the latter is the volume of water warmer than 20^oC in the equatorial Pacific (120^oE–80^oW, 5^oS–5^oN), which is a proxy for the thermocline depth and subsurface heat content (Meinen and McPhaden 2000). To predict DJF Niño 3.4 SST, WIO SST and WWV of each month from the January of previous year to the November of current year (Fig. 12, x-axis labels) are used as an input for the linear-regression forecast model, corresponding to lead times from 22 months to 0 month (Fig. 12, x-axis labels). The CFSv2 only provides 9-month lead forecasts, resulting in the DJF Niño 3.4 SST forecasts with lead times from 6 months (initialized in May) to 0 month (initialized in November).

The CFSv2 has the highest forecast skill at all available lead times (0–6 months) with all anomaly correlations above 0.7 (Fig. 12, black line). The skill of the statistical forecasts based on WWV (purple line) is lower than the dynamical forecasts, but the anomaly correlations are above the 99% significance level (0.48, solid gray line) at 0- to 10-month leads. There is a sharp decrease in the anomaly correlation at the 12-month lead, beyond which no skillful forecasts are found. The maximum lead of 12 months is likely determined by the time needed for subsurface temperature anomalies from the tropical western Pacific to cross the Pacific basin and reach the sea surface in the tropical eastern Pacific. When using the WIO SST as a predictor (red line), skillful forecasts are found at either a short lead time of 0 month (above the 99% significance level) or longer leads of 12–16 months (above the 95% significance level). The former is associated with the co-occurrence of IOD and ENSO (e.g., Fig. 1; Behera et al. 2006; Luo et al. 2010), whereas the latter is attributed to the signal of warm WIO SST anomalies appearing well ahead (> 1 year) of El Niño (Fig. 3). The skill of the WIO SST-based forecasts is lower than those of the CFSv2 and the WWV-based forecasts, but the lead time of skillful forecasts with the WIO SST is longer than the other two.

When using both WIO SST and WWV as predictors with a multiple linear regression model, the forecast skill (Fig. 12, green line) is comparable to that based solely on WWV (purple line) at lead times from 0 to 10 months, but is significantly improved at longer leads. For instance, the anomaly correlation skills of the WWV-based forecasts (purple line) are 0.50 and

0.10 at the 10-month and 13-month leads, respectively. The corresponding skills with the two predictors (green line) are 0.57 and 0.52. The results presented in Fig. 12 suggest that for the ENSO prediction, the statistical forecast based on WWV can extend the limit of lead time of the dynamical forecast from 6 months to 10 months. Using the WIO SST as an additional predictor can further extend the lead times of skillful forecasts up to 13 months (99% significance level) or 15 months (95% significance level). This is consistent with the findings of Wieners et al. (2016) that WIO may affect ENSO and an El Nino is preceded by the change in WIO SST about 15 month earlier.

Figure 12 also presents the forecast skills using the EIO SST and the IOD index as individual predictors. Comparing to the forecast skill with the WIO SST (red line), the skill with the EIO SST (yellow line) is slightly better at short leads, but much worse at long leads. Consistently, the skill with the IOD index (orange line), consisting of both the EIO and WIO SSTs is relatively high at short lead times, and degraded at long leads due to the EIO SST. As a result, the forecast skill is not significantly improved when adding the EIO SST to WWV at long leads (cyan line vs. purple line). The skill with WWV and IOD (blue line) is also not as good as that with WWV and WIO (green line) at long leads. Clearly, the improvement of ENSO prediction at long leads (10–15 months) is attributable to the WIO SST.

How the WIO SST contributes to the ENSO prediction is further examined for the two big El Niño events (1997/98 and 2015/16). Figure 13 shows the predicted Niño 3.4 SST anomalies for DJF 1997/98 and 2015/16 with the linear regression model using both individual predictors (WWV, WIO SST) and two predictors (WWV + WIO SST) at lead times from 22 months to 0 month. The observed values of the Niño 3.4 index are 2.50 K and 2.56 K for DJF 1997/98 and DJF 2015/16, respectively. All forecasts with a maximum value of 1.7 K in Fig. 13

are weaker than the observed. If El Niño is defined by the Niño 3.4 index with a threshold of 0.5 K (e.g., Trenberth 1997), the 1997/98 and 2015/16 events could be predicted at lead times of 11 and 10 months, respectively, using WWV as the predictor (Fig. 13, blue bars). Adding the WIO SST as an extra predictor extends the maximum lead time for forecasting El Niño to 16 and 11 months (Fig. 13, green bars), respectively, for the two events. Additionally, the WIO SST helps ENSO prediction not only at long leads, but also at short leads (0–2 months) by increasing the magnitude of the predicted Niño 3.4 index (Fig. 13, red and green bars). This is consistent with the overall forecast skill assessed by the cross-validations (Fig. 12, red line). Figure 13 also suggests that the WIO SST improves the ENSO prediction more significantly for the 1997/98 El Niño than for the 2015/16 El Niño, especially at long lead times (11–16 months). The difference may be due to their different lead-lag relationships with IOD or the difference in the strength of the IOD itself. For the 1997/98 event, the projection of surface and subsurface ocean temperatures onto EEOF2 (–2.45) is more than onto EEOF1 (1.83), whereas for the 2015/16 events, the projection onto EEOF1 (1.36) is more than onto EEOF2 (–1.14), based on the EEOF analysis of the GODAS data (not shown). Indeed, a recent study by Mayer et al. (2018) discloses different energetics of the 1997/98 and 2015/16 El Nino events in relation to the Indian Ocean.

Possible mechanisms responsible for the influence of IOD on ENSO have been discussed in some previous studies via both the atmospheric bridge and oceanic pathway (e.g., Wijffels and Meyers 2004; Annamalai et al. 2005; Izumo et al. 2010; Wieners et al. 2016). The atmospheric processes involve changes in the low-level zonal wind over the equatorial Pacific through the Walker Circulation or via the Philippine Sea anticyclone. More specifically, warm SST anomaly in WIO enhances local convection, which leads to suppressed convection over Indonesia and a weakened Walker Circulation over the tropical Pacific sector. Alternatively, perturbations to the Philippine Sea anticyclone generate a Kelvin wave which can also alter the western Pacific circulation. Both processes are invoked as modulators of the surface zonal wind in the tropical Pacific and thus capable of affecting the development of ENSO.

4. Conclusions and discussions

In this study the coevolution of IOD and ENSO is assessed by analyzing and comparing two 500-year CFS coupled model simulations with and without ENSO. The EEOF analysis of surface and subsurface ocean temperatures in the tropical Indian Ocean and western Pacific from the ENSO run reveals strong covariability of IOD and ENSO that are closely related to the subsurface ocean variability across the two tropical ocean sectors. The first EEOF mode shows the development of a positive IOD that lags El Niño, while the second mode exhibits the transition from a positive IOD to a basin-wide warming that leads El Niño. The lead and lag relationships between IOD and ENSO are consistent with two-way interactions between them.

The impact of ENSO on IOD was examined through a comparison between the ENSO and no-ENSO runs. The results indicate that ENSO not only enhances the variability of IOD at the interannual time scale but also increases the amplitude of SST anomalies in the IOD regions. A further comparison between the SST variances in the regions of EIO and WIO discloses the asymmetries of the ENSO influence between the eastern and western poles and between the positive and negative IOD phases. Specifically, the influence of ENSO on the IOD intensity is larger for the eastern pole than for the western pole, and is stronger in a negative IOD phase than in a positive phase.

The impact of IOD on ENSO was demonstrated by the improvement of ENSO prediction when considering the WIO SST as an ENSO precursor. The improvement is found not only at a short lead time (0 month) but also at long leads (10–15 months). The WIO SST plays a much more important role than the EIO SST in improving ENSO prediction at long leads. The eastward propagating surface and subsurface temperature signals from the western Indian Ocean that precede the development of heat content anomaly in the tropical western Pacific are the key for extending the lead time for ENSO prediction. It is also shown that WIO SST helps ENSO prediction more effectively for the 1997/98 El Niño than for the 2015/16 El Niño, which is likely due to their different lead-lag relationships with IOD and the strength of IOD between the two ENSO events.

A recent study by Saji (2018) argues that the basinwide SST anomalies in the tropical Indian Ocean induced by ENSO are zonally nonuniform. The impact of ENSO thus cannot be removed by the difference between the WIO and EIO SST anomalies in constructing the IOD index. A similar EEOF analysis was performed using the tropical ocean temperature anomalies after removing the ENSO signal by using 5-month lagged regression with the Niño 3.4 index, similar to what Saji and Yamagata (2003b) did, for the tropical Indian Ocean temperature east of 120^{o}E. The IOD signals are significantly weakened in the two leading EEOFs that covary with ENSO (not shown). The results show the importance of the ENSO impact on the IOD-ENSO association.

Therefore, it should be noted that the two-way interactions between ENSO and IOD may not be equally important and the impact of IOD on ENSO may depend on the mean state (see Annamalai et al. 2005; Chen 2010). Given that ENSO is a major source of interannual variability in the atmosphere-ocean system, its impact on IOD contributes significantly to the variability of IOD. In contrast, the impact of IOD should be less important to ENSO (Chen 2010). Additionally, based on a wavelet analysis with the 480-year PC time series of EEOF1 and EEOF2, the co-variability between ENSO and IOD exhibits variations on decadal timescales (not shown; see Ashok et al. 2003a; Annamalai et al. 2005). Specifically, the co-variability is strong in some decades, but weak in some other decades.

It should also be noted that the results presented in this paper are specific to the CFS model alone and the EEOF method used. Therefore, there might be some limitations, depending on the fidelity of the CFS in reproducing the mean IOD and ENSO, as well as their covariability. Previous studies reveal that the CFS can reproduce the observed features of both the IOD and ENSO reasonably well (e.g., Kim et al. 2012; Wang et al. 2016). Consistently, to some extent, the covariations between the IOD and ENSO identified in the CFS simulations are similar to those in GODAS.

The physical processes responsible for the interaction between IOD and ENSO may involve the teleconnection through the atmospheric "bridge" (e.g., the Walker circulation, the Philippine Sea anticyclone and Indonesian precipitation, Klein et al. 1999; Kumar and Hoerling 2003; Annamalai et al. 2005; Hendon 2013; Wieners et al. 2017b), the air-sea coupled mechanisms and thermocline feedback (e.g., Lu et al. 2018), and/or ocean internal processes (e.g., the Indonesian Throughflow, Wang et al. 2004; Zhou et al. 2015; Mayer et al. 2018). Further studies will be needed to understand the ENSO and IOD events where this covariability is not obvious and whether the preconditioning of the EIO may play a role in the strength of the covariability (Annamalai et al. 2005). Further analysis is also needed for understanding the role of these IOD-ENSO interactions on processes such as the recharge-discharge which are argued to be fundamental for ENSO events (Jin 1997, Ramesh and Murtugudde 2013) and the likely dependence of ENSO flavors on the role of IOD in ENSO (Capotondi et al. 2015; Wieners et al. 2017a) or the impact of Indian Ocean warming on the ENSO-IOD covariability (Lee et al. 2015).

Also of interest would be the Indo-Pacific Tripole framework proposed by Chen and Cane (2008) which may offer further process understanding of the relationship between the two basins. Further diagnoses of observations and the two simulations are required to understand the dynamics of the lead and lag linkages between IOD and ENSO documented in this study. It is nonetheless evident that the details of the evolution of warm and cold ENSOs and the positive and negative IODs represent advancement in the process understanding with demonstrable improvements in ENSO predictions.

Acknowledgments The authors would like to thank three anonymous reviewers and the editor for their insightful and constructive comments and suggestions.

Appendix

Quasi-biennial periodicity of the IOD

Previous studies (e.g., Saji et al. 1999) reveal that the IOD has a quasi-biennial variation. However, a near 2-year peak is not found in the power spectrum of the IOD in GODAS (Fig. 8a). Instead, there is a minimum power at 2 years, which is also different from the model results (Fig. 6b). One possibility that could cause the difference in the peaks between the model and GODAS is data sampling issue. For example, the power spectrum of the 480-year IOD index in the ENSO run (Fig. 6b, red line) is the average of the power spectra for 8 × 60 years. Figure A1 shows the individual spectrum for each 60 years, in addition to their average (red line). Among the eight members, there are large inter-member spreads in the power spectra. In particular, there is one with a peak at 2 years (green) and another one with a minimum at 2 years (blue). Given that the IOD index derived from the 36-year GODAS data has only one realization, it is not surprising to see the difference in the peaks at some specific periods (here 2 years) between the model and GODAS.

References

Allan R, Chambers D, Drosdowsky W, Hendon H, Latif M, Nicholls N, Smith I, Stone R, Tourre Y (2001) Is there an Indian Ocean dipole, and is it independent of the El Niño-Southern Oscillation? CLIVAR Exchanges, 6:18–22

Annamalai H, Murtugudde R (2004) Role of the Indian Ocean in regional climate variability. Earth Climate: The Ocean-Atmosphere Interaction, Wang C, Xie S-P, Carton JA (eds.), AGU Geophysical Monograph 147:213–246

Annamalai H, Murtugudde R, Potemra J, Xie SP, Liu P, Wang B (2003) Coupled dynamics over the Indian Ocean: Spring initiation of the zonal mode. Dee-Sea Res II 50:2305–2330. doi:10.1016/S0967-0645(03)00058-4

Annamalai H, Xie SP, McCreary JP, Murtugudde R (2005) Impact of Indian Ocean sea surface temperature on developing El Niño. J Clim 18:302–319

Ashok K, Guan Z, Yamagata T (2001) Impact of the Indian Ocean dipole on the relationship between the Indian monsoon rainfall and ENSO. Geophys Res Lett 28:4499–4502

Ashok K, Guan Z, Yamagata T (2003a) A look at the relationship between the ENSO and the Indian Ocean dipole. J Meteor Soc Japan 81:41–56

Ashok K, Guan Z, Yamagata T (2003b) Influence of the Indian Ocean dipole on the Australian winter rainfall. Geophys Res Lett 30:1821. doi:10.1029/2003GL017926

Ashok K, Guan Z, Saji NH, Yamagata T (2004) Individual and combined influence of ENSO and the Indian Ocean dipole on the Indian summer monsoon. J Clim 17:3141–3155

Behera SK, Luo JJ, Masson S, Delecluse P, Gualdi S, Navarra A, Yamagata T (2005) Paramount impact of the Indian Ocean dipole on the East African short rains: A CGCM study. J Clim 18:4514–4530

Behera SK, Luo JJ, Masson S, Rao SA, Sakuma H, Yamagata T (2006) A CGCM study on the interaction between IOD and ENSO. J Clim 19:1688–1705

Behringer DW, Xue Y (2004) Evaluation of the global ocean data assimilation system at NCEP: The Pacific Ocean. Eighth Symp. on Integrated Observing and Assimilation Systems for Atmosphere, Oceans, and Land Surface, Seattle, WA, Amer. Meteor. Soc. [Available online at http://ams.confex.com/ams/84Annual/techprogram/paper_70720.htm]

Bjerknes J (1969) Atmospheric teleconnections from the equatorial Pacific. Mon Wea Rev 97:163–172

Cadet DL (1985) The Southern Oscillation over the Indian Ocean. J Climatol 5:189–212

Capotondi A et al. (2015) Understanding ENSO diversity. Bull Amer Meteor Soc 96:921–938

Chen D (2010) Indo-Pacific tripole: An intrinsic mode of tropical climate variability. Adv Geosci 24, Ocean Science, 18pp

Chen D, Cane MA (2008) El Nino prediction and predictability. J Comput Phys 227:3625–3640

Cherchi A, Navarra A (2013) Influence of ENSO and of the Indian Ocean dipole on the Indian summer monsoon variability. Clim Dyn 41:81–103

Dayan H, Vialard J, Izumo T, Lengaigne M (2014) Does sea surface temperature outside the tropical Pacific contribute to enhanced ENSO predictability? Clim Dyn 43:1311–1325

Drbohlav H-KL, Gualdi S, Navarra A (2007) A diagnostic study of the Indian Ocean dipole mode in El Niño and non-El Niño years. J Clim 20:2961–2977

Du Y, Cai W, Wu Y (2013) A new type of the Indian Ocean dipole since the mid-1970s. J Clim 26:959–972

Hendon HH (2003) Indonesian rainfall variability: Impact of ENSO and local air–sea interaction. J Clim 16:1775–1790

Izumo T et al (2010) Influence of the state of the Indian Ocean dipole on the following year's El Nino. Nat Geosci 3:168–172

Izumo T, Lengaigne M, Vialard J, Luo JJ, Yamagata T, Madec G (2014) Influence of Indian Ocean dipole and Pacific recharge on flowing year's El Nino: interdecadal robustness. Clim Dyn 42:291–310

Izumo T, Vialard J, Dayan H, Lengaigne M, Suresh I (2016) A simple estimation of equatorial Pacific response from windstress to untangle Indian Ocean dipole and basin influences on El Niño. Clim Dyn 46:2247–2268

Jin F-F (1997) An equatorial ocean recharge paradigm for ENSO. Part I: Conceptual model. J Atmos Sci 54:811–829

Jourdain NC, Lengaigne M, Vialard J, Izumo T, Gupta AS (2016) Further indights on the influence of the Indian Ocean dipole on the following year's ENSO from observations and CMIP5 models. J Clim 29:637–658

Kim ST, Yu J-Y, Kumar A, Wang H (2012) Examination of the two types of ENSO in the NCEP CFS model and its extratropical associations. Mon Wea Rev 140:1908–1923

Klein SA, Soden BJ, Lau NC (1999) Remote sea surface temperature variations during ENSO: Evidence for a tropical atmospheric bridge. J Clim 12:917–932

Kumar A, Hoerling MP (2003) The nature and causes for the delayed atmospheric response to El Niño. J Clim 16:1391–1403

Kumar A, Wang H (2015) On the potential of extratropical SST anomalies for improving climate prediction. Clim Dyn 44:2557–2569

Kumar A, Wang H, Wang W, Xue Y, Hu Z-Z (2013) Does knowing the oceanic PDO phase help predict the atmospheric anomalies in subsequent months? J Clim 26:1268–1285

Latif M, Barnett TP (1995) Interactions of the tropical oceans. J Clim 8:952–964

Lee S-K, Park W, Baringer MO, Gordon AL, Huber B, Liu Y (2015) Pacific origin of the abrupt increase in Indian Ocean heat content during the warming hiatus. Nature Geosci 8:445–449

Li CY, Mu MQ (2001) Influence of the Indian Ocean dipole on atmospheric circulation and climate. Adv Atmos Sci 18:831–843

Liu J, Wang H, Lu E, Kumar A (2017) Decadal modulation of East China winter precipitation by ENSO. Clim Dyn doi:10.1007/s00382-016-3427-6

Lu B, Ren H-L, Scaife AA, Wu J, Dunstone N, Smith D, Wan J, Eade R, MacLachlan C, Gordon M (2018) An extreme negative Indian Ocean Dipole event in 2016: dynamics and predictability. Clim Dyn 51:89–100

Luo JJ, Masson S, Behera SK, Yamagata T (2008) Extended ENSO predictions using a fully coupled ocean–atmosphere model. J Clim 21:84–93

Luo JJ, Zhang R, Behera SK, Masumoto Y, Jin F-F, Lukas R, Yamagata T (2010) Interaction between El Nino and extreme Indian Ocean dipole. J Clim 23:726–742

Mayer M, Balmaseda MA, Haimberger L (2018) Unprecedented 2015/2016 Indo-Pacific heat transfer speeds up tropical Pacific heat recharge. Geophys Res Lett 45:3274–3284

Meinen CS, McPhaden MJ (2000) Observations of warm water volume changes in the equatorial Pacific and their relationship to El Niño and La Niña. J Clim 13:3551–3559

Moorthi S, Pan H-L, Caplan P (2001) Changes to the 2001 NCEP operational MRF/AVN global analysis/forecast system. NWS technical procedures bulletin no. 484, 14 pp.

Murtugudde R, Busalacchi AJ (1999) Interannual variability of the dynamics and thermodynamics of the Indian Ocean. J Clim 12:2300–2326

Murtugudde R, McCreary J, Busalacchi AJ (2000) Oceanic processes associated with anomalous events in the Indian Ocean with relevance to 1997-98. J Geophys Res 105:3295–3306

Okumura YM, Deser C (2010) Asymmetry in the duration of El Niño and La Niña. J Clim 23:5826–5843

Pacanowski RC, Griffies SM (1998) MOM 3.0 manual. NOAA/GFDL 668 pp

Pan H-L, Mahrt L (1987) Interaction between soil hydrology and boundary layer developments. Bound-Layer Meteor 38:185–202

Ramesh N, Murtugudde R (2013) All flavors of El Niño have similar subsurface origins. Nature Clim Change 3:42–46

Reynolds RW, Rayner NA, Smith TM, Stokes DC, Wang W (2002) An improved in situ and satellite SST analysis for climate. J Clim 15:1609–1625

Saha S et al (2006) The NCEP climate forecast system. J Clim 19:3483–3517

Saha S et al (2014) The NCEP climate forecast system version 2. J Clim 27:2185–2208

Saji NH (2018) The Indian Ocean Dipole. Oxford Research Encyclopedia of Climate Science, doi:10.1093/acrefore/9780190228620.013.619

Saji NH, Goswami BN, Vinayachandran PN, Yamagata T (1999) A dipole mode in the tropical Indian Ocean. Nature 401:360–363

Saji NH, Yamagata T (2003a) Possible impacts of Indian Ocean dipole mode events on global climate. Clim Res 25:151–169

Saji NH, Yamagata T (2003b) Structure of SST and surface wind variability during Indian Ocean dipole mode events: COADS observations. J Clim 16:2735–2751

Snedecor GW, Cochran WG (1989) Statistical Methods, 8th edn. Iowa State Univ. Press, p503

Stuecker MA, Timmermann A, Jin F-F, Chikamoto Y, Zhang W, Wittenberg AT, Widiasih E, Zhao S (2017) Revisiting ENSO/Indian Ocean Dipole phase relationships. Geophys Res Lett 44:2481–2492

Tamura T, Koike T, Yamamoto A, Yasukawa A, Kitsuregawa M (2011) Contrasting impacts of the Indian Ocean dipole and ENSO on the tropospheric biennial oscillation. SOLA 7:13–16

Trenberth KE (1997) The definition of El Niño. Bull Amer Meteor Soc 78:2771–2777

Wallace JM, Rasmusson EM, Mitchell TP, Kousky VE, Sarachik ES, von Storch H (1998) On the structure and evolution of ENSO-related climate variability in the tropical Pacific. J Geophys Res 103:14241–14260

Wang DX, Liu QY, Liu Y, Shi P (2004) Connection between interannual variability of the western Pacific and eastern Indian Oceans in the 1997–1998 El Niño event. Prog Nat Sci 14: 423–429

Wang H, Kumar A (2015) Assessing the impact of ENSO on drought in the U.S. Southwest with the NCEP climate model simulations. J Hydrol 526:30–41. doi:10.1016/j.jhydrol.2014. 12. 012

Wang H, Kumar A, Wang W (2013) Characteristics of subsurface ocean response to ENSO assessed from simulations with the NCEP climate forecast system. J Clim 26:8065–8083

Wang H, Kumar A, Wang W, Xue Y (2012a) Seasonality of the Pacific decadal oscillation. J Clim 25:25–38

Wang H, Kumar A, Wang W, Xue Y (2012b) Influence of ENSO on Pacific decadal variability: An analysis based on the NCEP Climate Forecast System. J Clim 25:6136–6151

Wang H, Murtugudde R, Kumar A (2016) Evolution of Indian Ocean dipole and its forcing mechanisms in the absence of ENSO. Clim Dyn 47:2481–2500

Wang H, Pan Y, Kumar A, Wang W (2013) Modulation of convectively coupled Kelvin wave activity in the tropical Pacific by ENSO. Acta Meteoro Sinica 27:295–307

Weare BC, Nasstrom JS (1982) Examples of extended empirical orthogonal function analysis. Mon Wea Rev 110:481–485

Webster PJ, Moore AM, Loschning JP, Leben RR (1999) Coupled ocean-atmosphere dynamics in the Indian Ocean during 1997–98. Nature, 401:356–360

Wieners CE, de Ruijter WPM, Ridderinkhof W, von der Heydt AS, Dijkstra HA (2016) Coherent tropical Indo-Pacific interannual climate variability. J Clim 29:4269–4291

Wieners CE, Dijkstra HA, de Ruijter WPM (2017a) The influence of the Indian Ocean on ENSO stability and flavor. J Clim 30:2601–2620

Wieners CE, Dijkstra HA, de Ruijter WPM (2017b) The influence of atmospheric convection on the interaction between the Indian Ocean and ENSO. J Clim 30:10155–10178

Wijffels SE, Meyers GM (2004) An intersection of oceanic wave guides: variability in the Indonesian throughflow region. J Phys Oceanogr 34:1232–1253

Wu R, Kirtman BP (2004) Understanding the impacts of the Indian Ocean on ENSO variability in a coupled GCM. J Clim 17:4019–4031

Xiao ZN, Yan HM, Li CY (2002) The relationship between Indian Ocean SSTA dipole index and the precipitation and temperature over China. J Tropical Meteor 18:335–344 (**in Chinese**)

Xie S-P, Hu K, Hafner J, Tokinaga H, Du Y, Huang G, Sampe T (2009) Indian Ocean capacitor effect on Indo-Western Pacific climate during the summer following El Niño. J Clim 22:730–747

Zhou Q, Duan W, Mu M, Feng R (2015) Influence of positive and negative Indian Ocean dipoles on ENSO via the Indonesian Throughflow: Results from sensitivity experiments. Adv Atmos Sci 32:783–793

Table 1 Number of SON seasons and percentage of co-occurrence for different phases of IOD and ENSO. Both ENSO and IOD events are defined using their corresponding standard deviation of the 480-year SON time series. Please see the main text for details.

Co-occurrence	Number of SON Seasons	Percentage of Co-occurrence
Positive IOD & El Niño	29	27% (29 out of 108)
Negative IOD & La Niña	35	39% (35 out of 90)
Positive IOD & La Niña	5	5% (5 out of /108)
Negative IOD & El Niño	4	4% (4 out of 90)

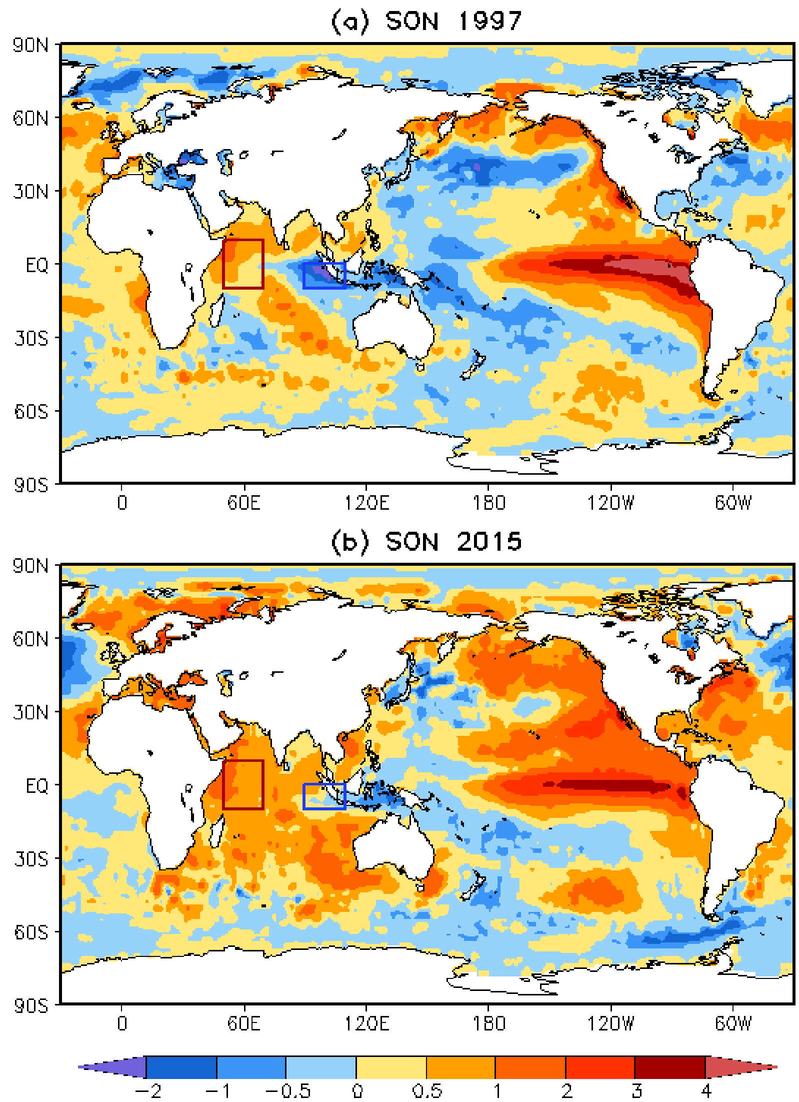

Fig. 1 Distribution of seasonal mean SST anomaly (K) in (**a**) SON 1997 and (**b**) SON 2015. The red and blue boxes denote the domains of WIO (50°–70°E, 10°S–10°N) and EIO (90°–110°E, 10°S–Eq.) used for averaging SST anomalies for the IOD index.

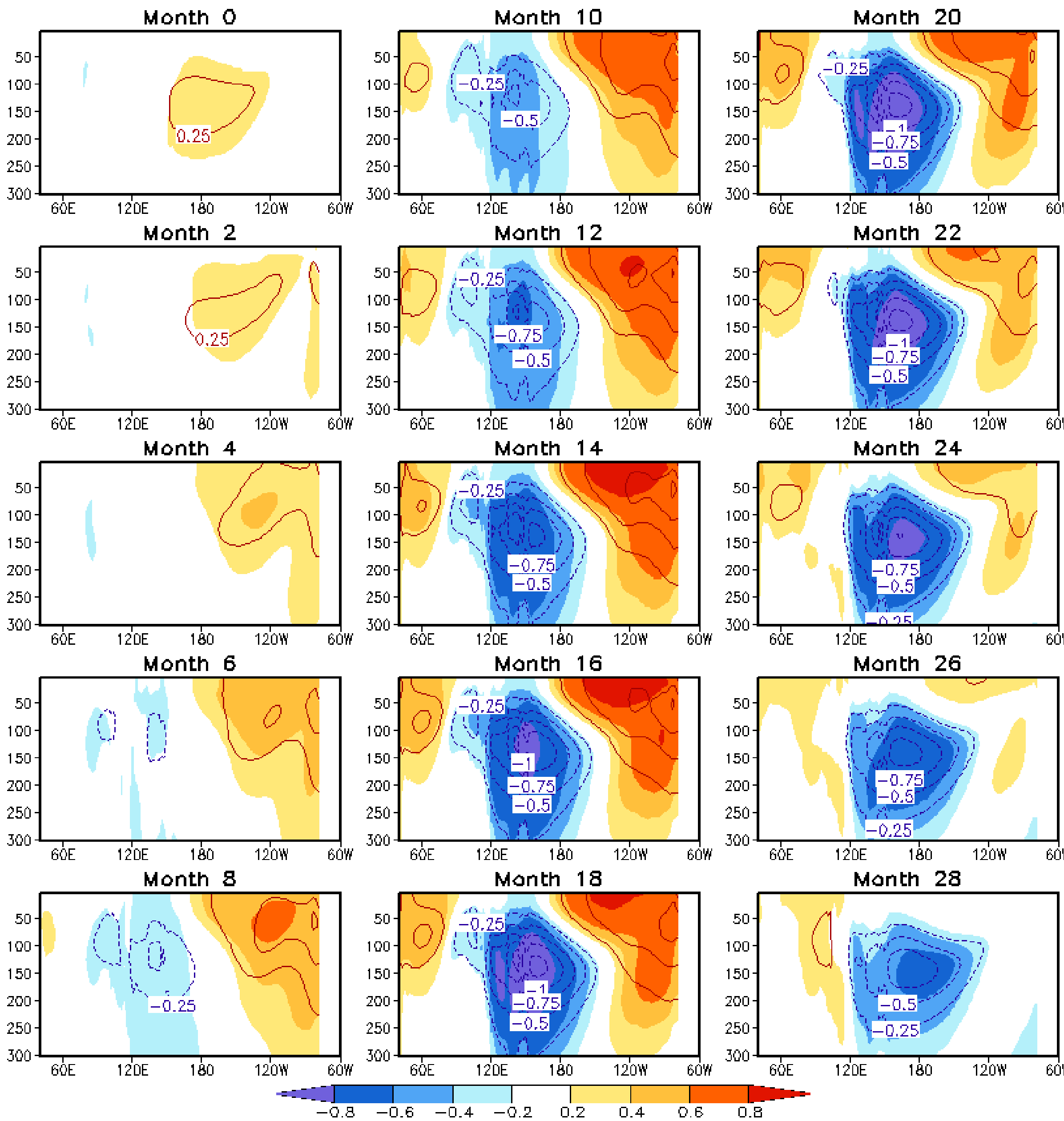

Fig. 2 Correlation (shading) and regression (contour) coefficients of monthly mean ocean temperature averaged over 10°S–5°N against the PC time series of the first EEOF from month 0 to month 28. Month 28 denotes ocean temperature lagging PC1 by 28 months. Contour interval is 0.25 K with negative values dashed and zero contours omitted. Correlations exceeding ±0.2 with shadings are above the 99% significance level, estimated by the two-tailed t-test (Snedecor and Cochran 1989).

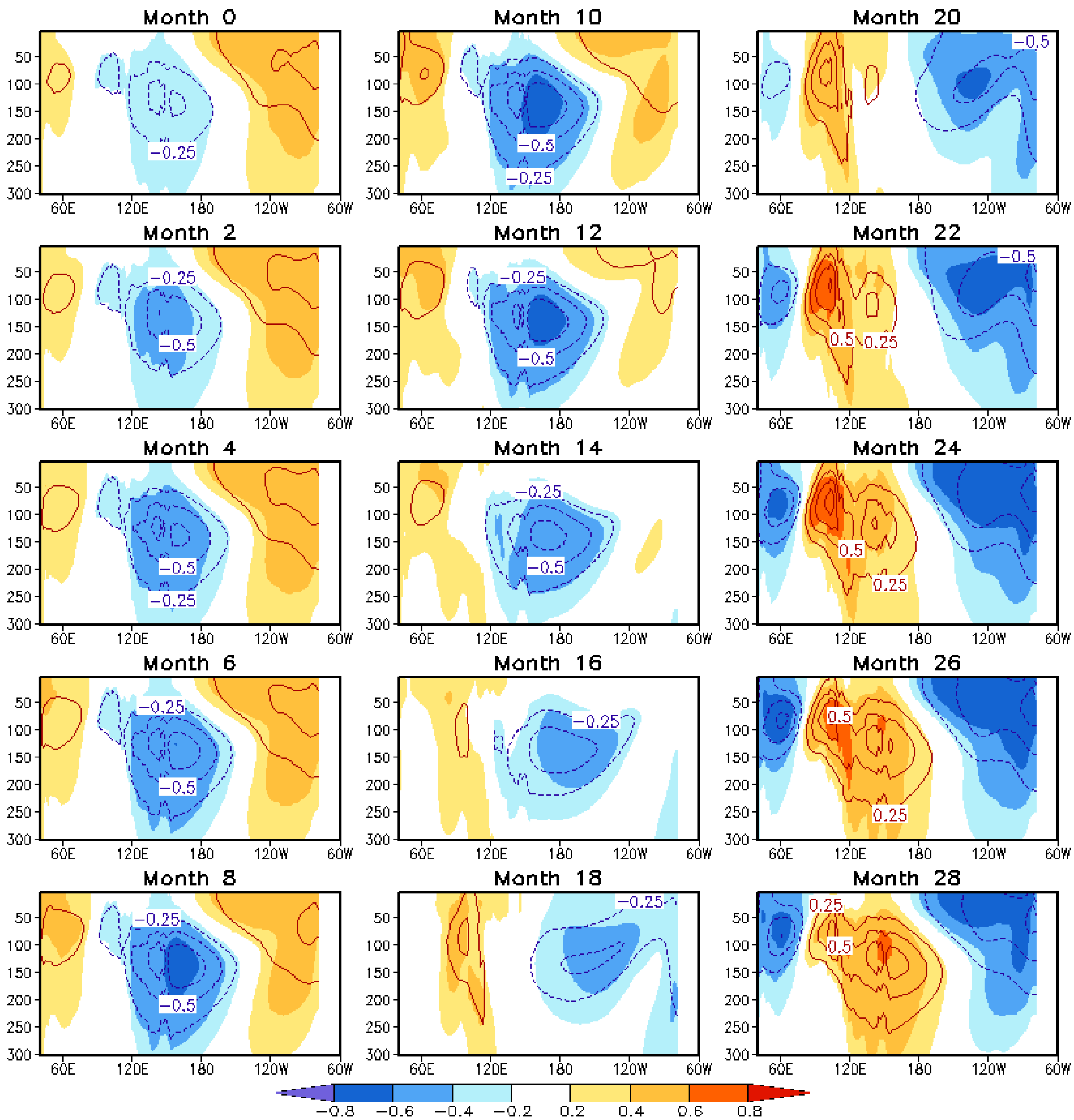

Fig. 3 Same as Fig. 2 but for the second EEOF.

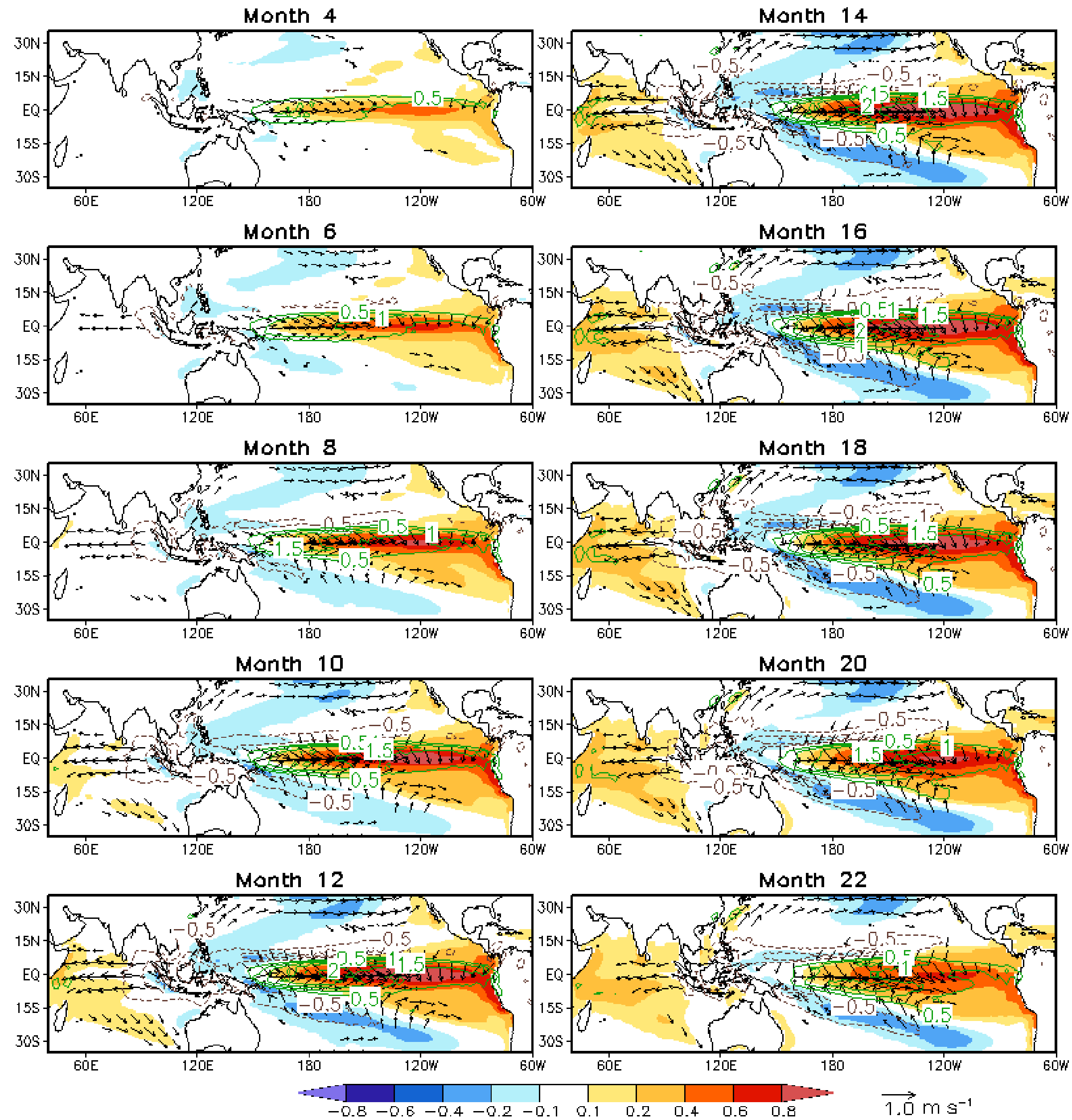

Fig. 4 SST (shading, K), 10-m wind (vector, m s^{-1}), and precipitation (contour, mm day^{-1}) anomalies associated with a one-standard-deviation departure in the PC1 time series obtained by regressing 480-year monthly fields against the time series of EEOF1 in the ENSO run from month 4 to month 22. Contour interval is 0.5 mm day^{-1} with green for positive values, dark brown for negative values (dashed), and zero contours omitted. Wind anomalies are plotted only over the oceans with anomalous wind speeds larger than 0.25 m s^{-1}.

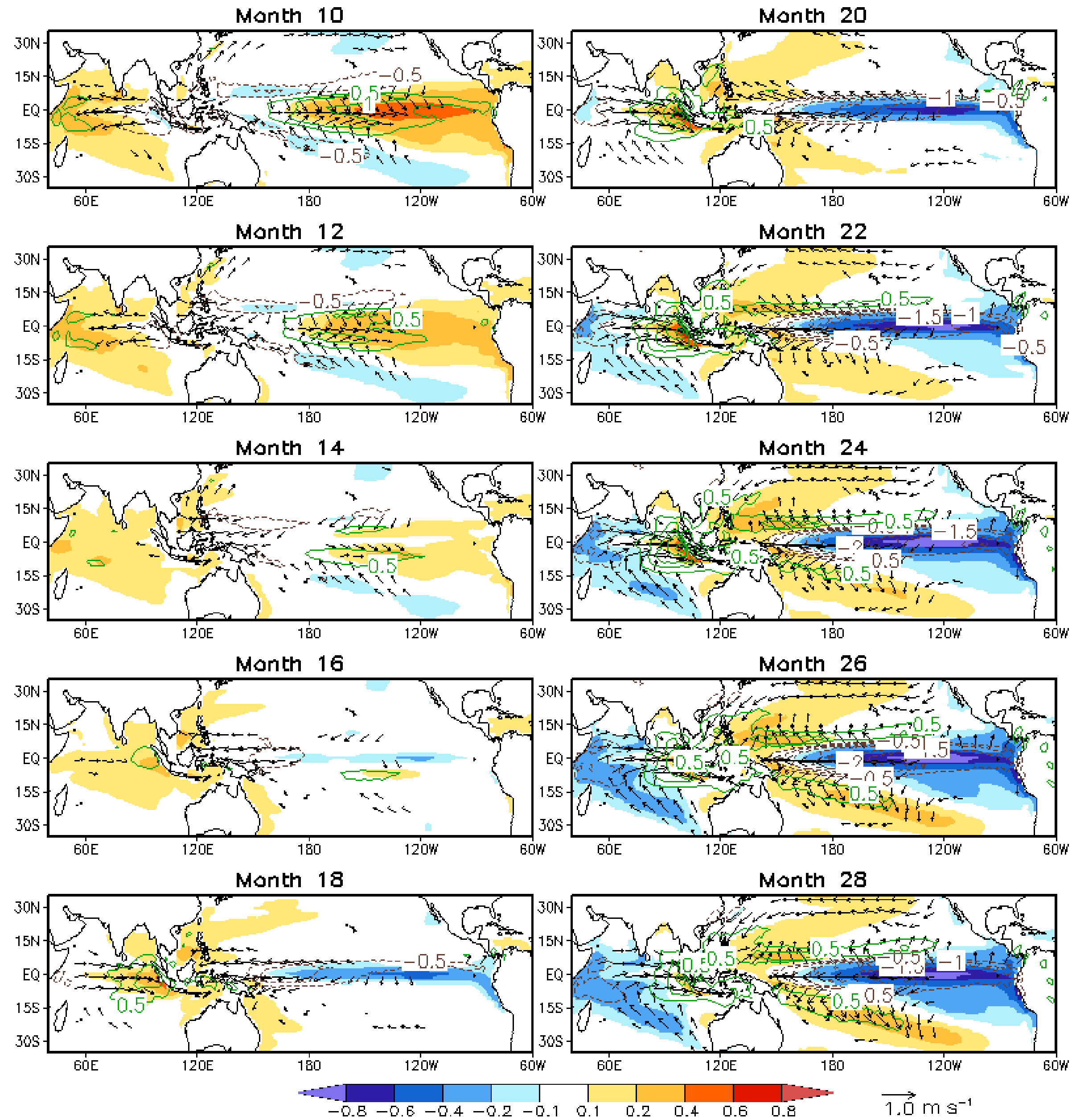

Fig. 5 Same as Fig. 4 but for the second EEOF from month 10 to month 28.

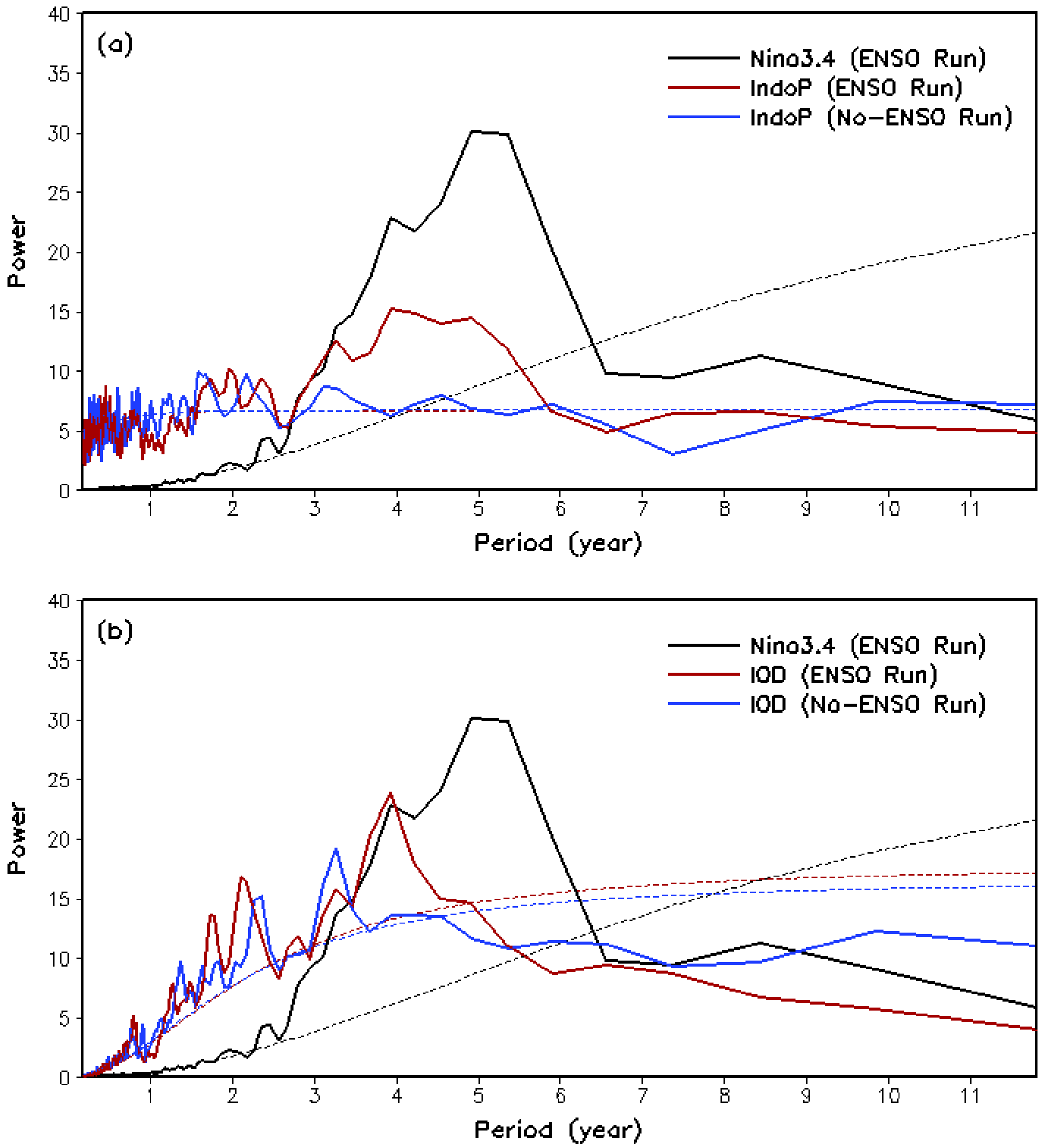

Fig. 6 Power spectra of the normalized 480-year time series of (**a**) the Niño 3.4 index in the ENSO run (black) and the IndoP index in the ENSO run (red) and no-ENSO run (blue), and (**b**) the Niño 3.4 index in the ENSO run (black) and the IOD index in the ENSO run (red) and no-ENSO run (blue). Dashed lines are corresponding red-noise spectra. The power spectra are averages over eight 60-year segments. The power spectra of the IndoP index and the IOD index are multiplied by a factor of 5 and 2, respectively, for display purposes only.

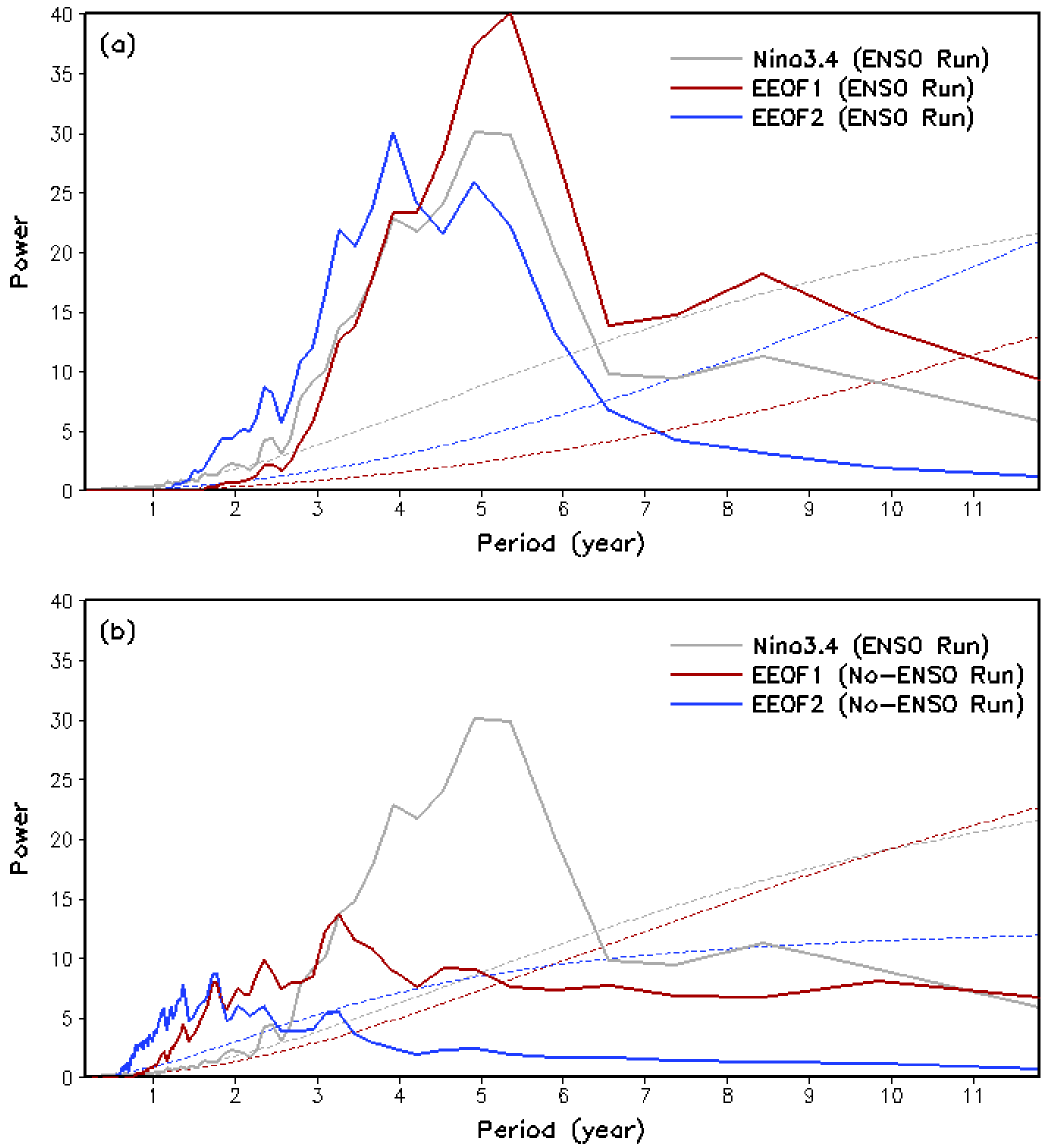

Fig. 7 Power spectra of the normalized 480-year time series of (**a**) the Niño 3.4 index in the ENSO run (grey) and the PCs of EEOF1 (red) and EEOF2 (blue) in the ENSO run and (**b**) in the no-ENSO run. Dashed lines are corresponding red-noise spectra. The power spectra are the averages over eight 60-year segments.

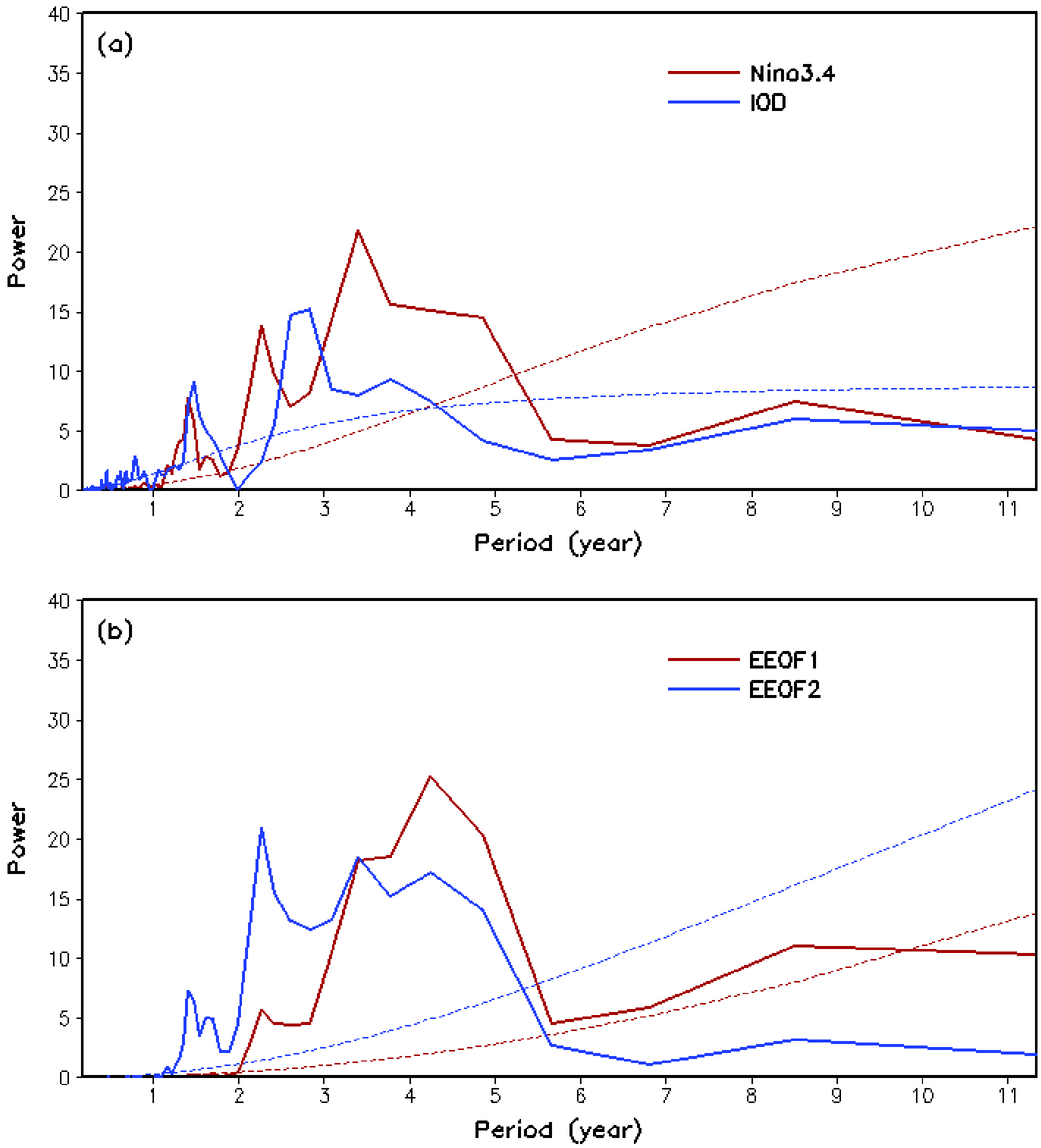

Fig. 8 Power spectra of the normalized 36-year time series of (**a**) the Niño 3.4 index and the IOD index and (**b**) the PCs of EEOF1 (red) and EEOF2 (blue) in GODAS. Dashed lines are corresponding red-noise spectra.

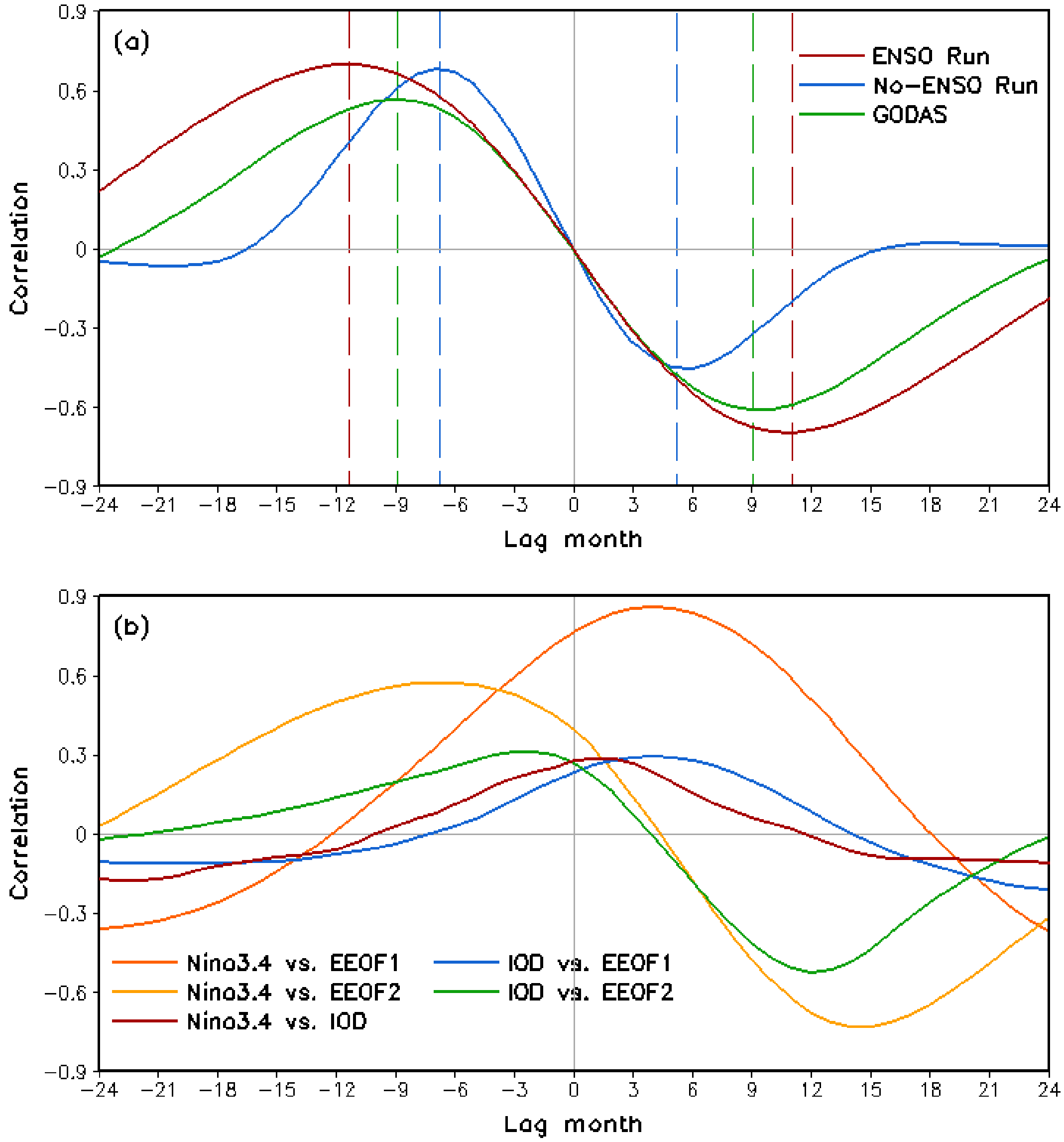

Fig. 9 (**a**) Lead and lag correlations between the two PC time series of EEOF1 and EEOF2 in the ENSO run (red solid line), no-ENSO run (blue solid line), and GODAS (green solid line) for EEOF1 leading EEOF2 24 months (lag month = –24) to EEOF1 lagging EEOF2 24 months (lag month = 24), and (**b**) similar lead and lag correlations of the Nino 3.4 index with the two PC time series of EEOF 1 (orange) and EEOF2 (yellow), the IOD index with the two PC time series of EEOF1 (blue) and EEOF2 (green), and the Nino 3.4 index with the IOD index (red) in the ENSO run from lag month –24 to lag month 24, namely, from the Nino 3.4 index leading the IOD index 24 months to lagging 24 months, for example. Vertical dashed color lines in (**a**) denote the lag month of the largest positive and negative correlation coefficients.

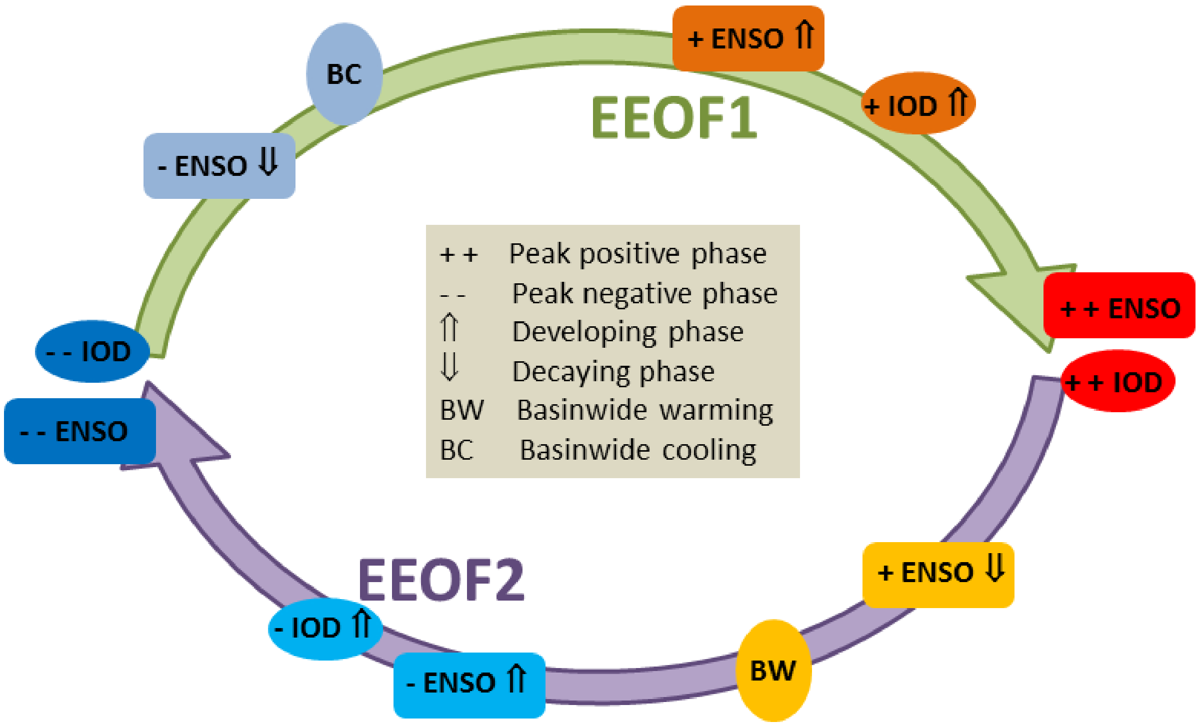

Fig. 10 Schematic of the covariations of ENSO and IOD through the alternation between EEOF1 and EEOF2. Signs + and – denote evolutionary phases.

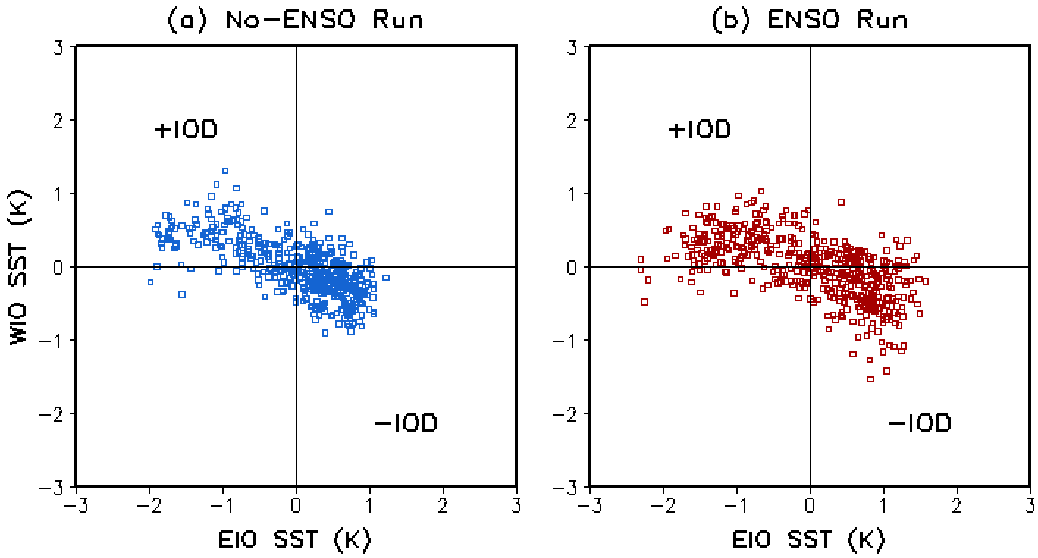

Fig. 11 Scatter plot of 480-year EIO SST versus WIO SST in SON for (**a**) the no-ENSO run and (**b**) the ENSO run.

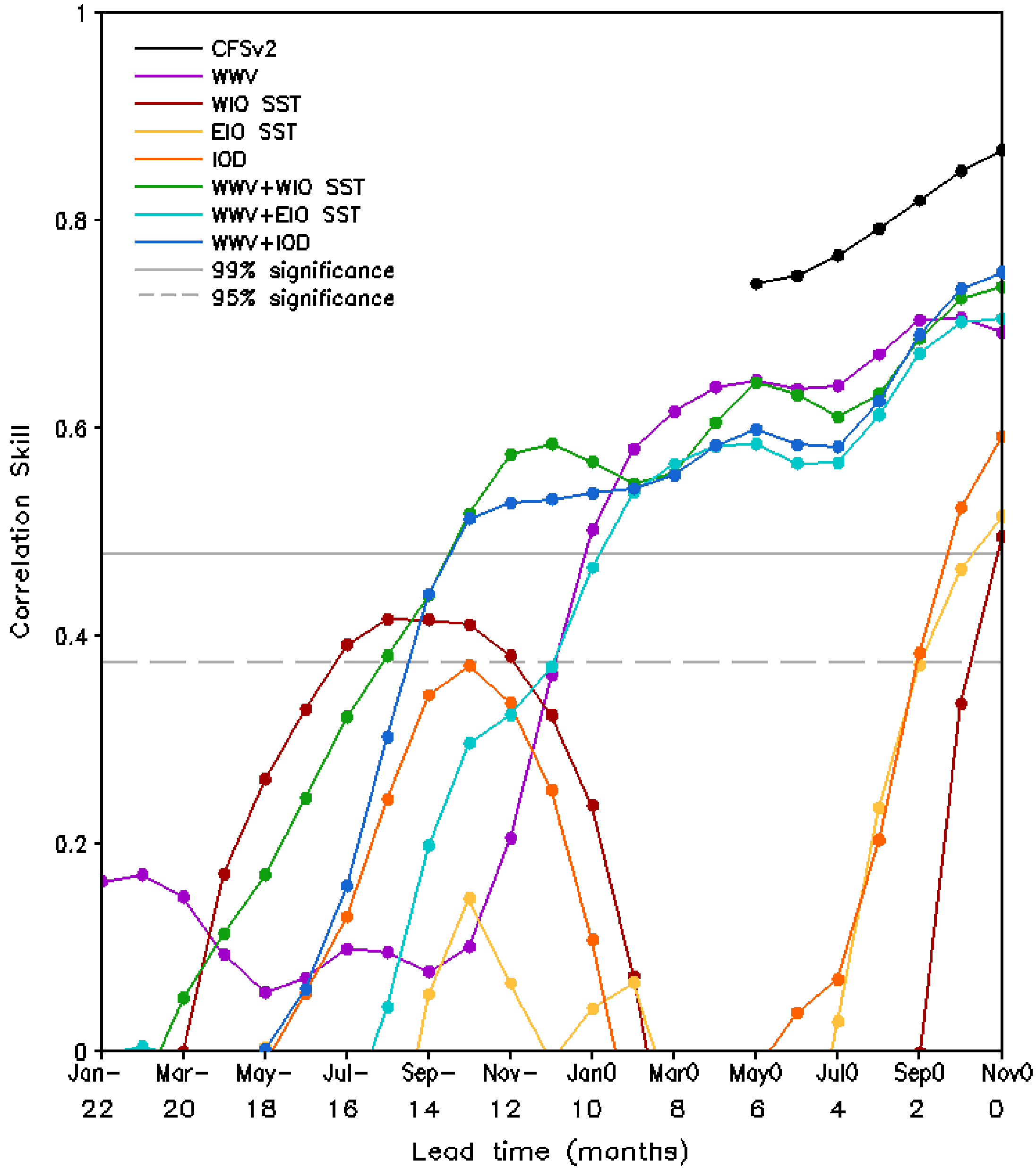

Fig. 12 Anomaly correlation skills of CFSv2 dynamical forecast (black) and statistical forecasts using one predictor (purple for WWV, red for WIO SST, yellow for EIO SST, orange for IOD index) and two predictors (green for WWV + WIO SST, cyan for WWV + EIO SST, blue for WWV + IOD) for DJF Niño 3.4 SST with lead times from 22 months to 0 month, corresponding to forecasts made from January of previous year to November of current year (Jan– to Nov0 with – and 0 for previous year and current year, respectively). Solid (dash) gray line denotes the threshold of the anomaly correlation at the 99% (95%) significance level.

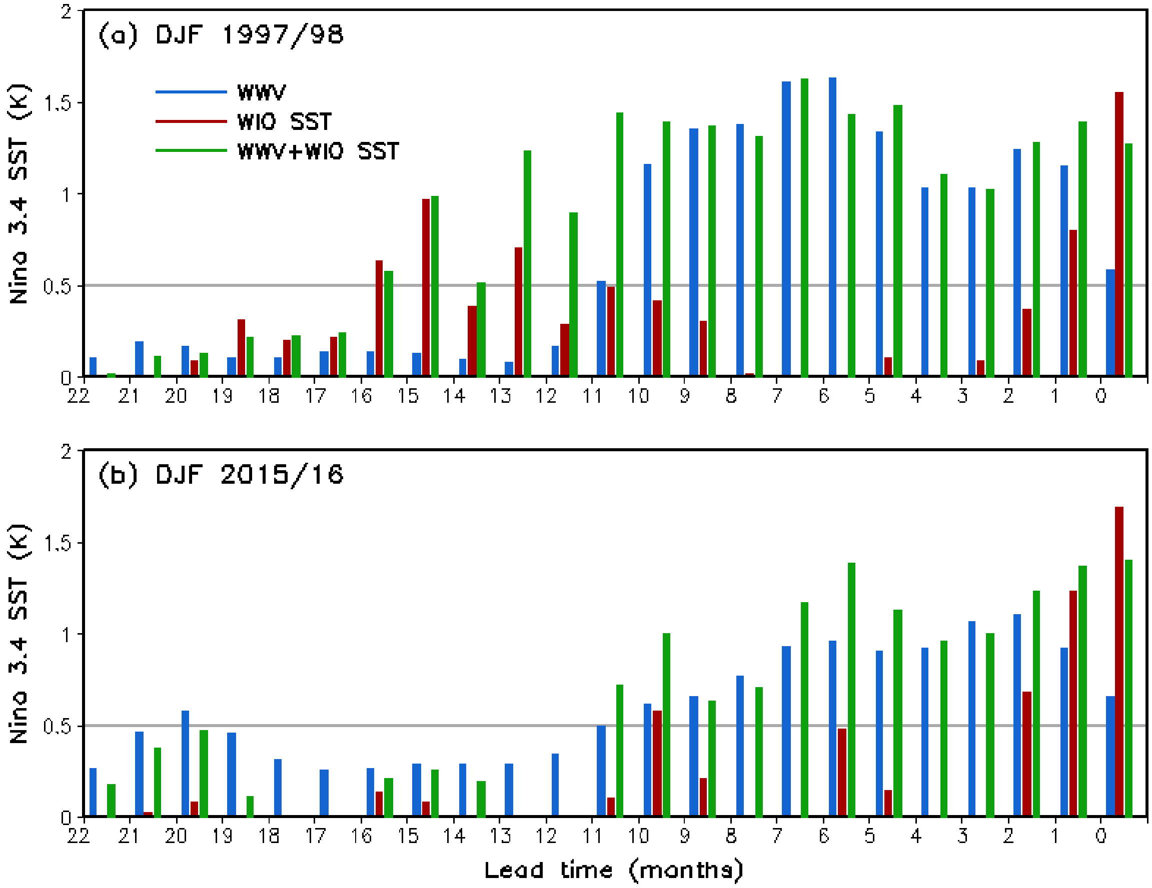

Fig. 13 Niño 3.4 SST anomalies (K) of (**a**) DJF 1997/98 and (**b**) DJF 2015/16 predicted by the linear regression model using one predictor (blue for WWV; red for WIO SST) and two predictors (WWV + WIO SST, green) with lead times from 22 months to 0 month. Gray line denotes the threshold (0.5 K) of the Niño 3.4 index for an El Niño.

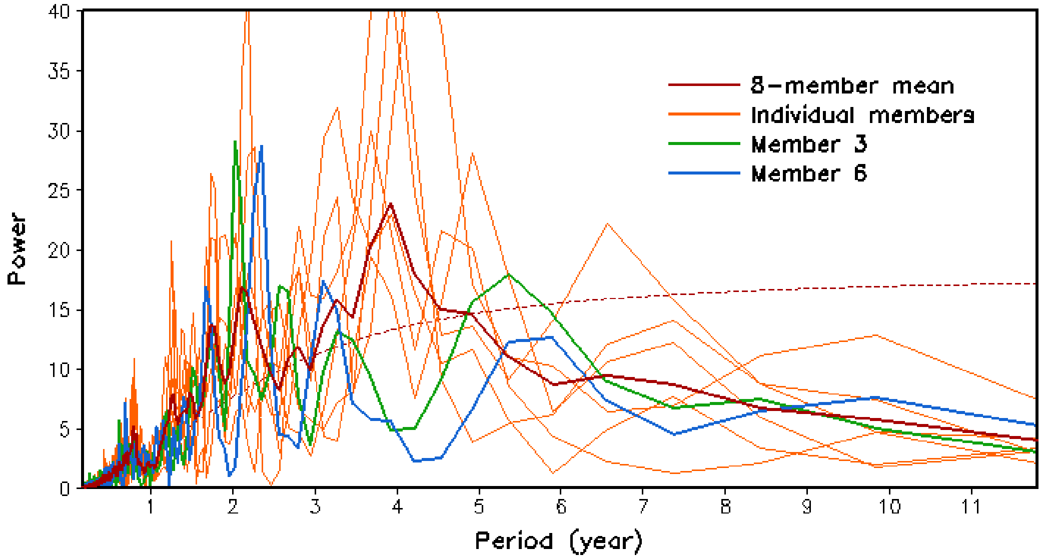

Fig. A1 Power spectra of the normalized 480-year time series of the IOD index in the ENSO run (red), which is the averages over eight 60-year segments, and those of eight individual 60-year segments (6 orange, 1 green, and 1 blue). Dashed line is the red-noise spectra.